



<b>Publication Year</b>	2018
<b>Acceptance in OA</b>	2020-12-28T16:03:00Z
<b>Title</b>	The Close AGN Reference Survey (CARS): SOFIA Detects Spatially Resolved [C II] Emission in the Luminous AGN HE 0433-1028
<b>Authors</b>	Busch, G., Husemann, B., Smirnova-Pinchukova, I., Eckart, A., Baum, S. A., Combes, F., Croom, S. M., Davis, T. A., Fazeli, N., Fischer, C., GASPARI, MASSIMO, Klein, R., Krumpke, M., McElroy, R., O'Dea, C. P., Perez-Torres, M. A., Powell, M. C., Sánchez-Monge, Á., Scharwächter, J., Tremblay, G. R., Urrutia, T.
<b>Publisher's version (DOI)</b>	10.3847/2041-8213/aae25d
<b>Handle</b>	<a href="http://hdl.handle.net/20.500.12386/29234">http://hdl.handle.net/20.500.12386/29234</a>
<b>Journal</b>	THE ASTROPHYSICAL JOURNAL LETTERS
<b>Volume</b>	866



# The Close AGN Reference Survey (CARS): SOFIA Detects Spatially Resolved [C II] Emission in the Luminous AGN HE 0433-1028\*

G. Busch<sup>1</sup> , B. Husemann<sup>2</sup> , I. Smirnova-Pinchukova<sup>2</sup> , A. Eckart<sup>1,3</sup> , S. A. Baum<sup>4,5</sup> , F. Combes<sup>6</sup> , S. M. Croom<sup>7</sup> , T. A. Davis<sup>8</sup> , N. Fazeli<sup>1</sup> , C. Fischer<sup>9</sup> , M. Gaspari<sup>10,20</sup> , R. Klein<sup>11</sup> , M. Krumpke<sup>12</sup> , R. McElroy<sup>2</sup> , C. P. O’Dea<sup>13,14</sup> , M. A. Perez-Torres<sup>15,16</sup> , M. C. Powell<sup>17</sup> , Á. Sánchez-Monge<sup>1</sup> , J. Scharwächter<sup>18</sup> , G. R. Tremblay<sup>19</sup> , and T. Urrutia<sup>12</sup>

<sup>1</sup> I. Physikalisches Institut der Universität zu Köln, Zùlpicher Str. 77, D-50937 Köln, Germany; [busch@ph1.uni-koeln.de](mailto:busch@ph1.uni-koeln.de)

<sup>2</sup> Max-Planck-Institut für Astronomie, Königstuhl 17, D-69117 Heidelberg, Germany; [husemann@mpia.de](mailto:husemann@mpia.de)

<sup>3</sup> Max-Planck-Institut für Radioastronomie, Auf dem Hügel 69, D-53121 Bonn, Germany

<sup>4</sup> Carlson Center for Imaging Science, Rochester Institute of Technology, 84 Lomb Memorial Drive, Rochester, NY 14623, USA

<sup>5</sup> Faculty of Science, University of Manitoba, Winnipeg, MB R3T 2N2, Canada

<sup>6</sup> LERMA, Observatoire de Paris, PSL Research Univ., Collège de France, CNRS, Sorbonne Univ., UPMC, Paris, France

<sup>7</sup> Sydney Institute for Astronomy, School of Physics, University of Sydney, NSW 2006, Australia

<sup>8</sup> School of Physics & Astronomy, Cardiff University, Queens Buildings, The Parade, Cardiff, CF24 3AA, UK

<sup>9</sup> Deutsches SOFIA Institut, Pfaffenwaldring 29, D-70569 Stuttgart, Germany

<sup>10</sup> Department of Astrophysical Sciences, Princeton University, 4 Ivy Lane, Princeton, NJ 08544-1001, USA

<sup>11</sup> SOFIA/USRA, NASA Ames Research Center, Moffett Field, California 94035, USA

<sup>12</sup> Leibniz-Institut für Astrophysik Potsdam, An der Sternwarte 16, D-14482 Potsdam, Germany

<sup>13</sup> Department of Physics & Astronomy, University of Manitoba, Winnipeg, MB R3T 2N2, Canada

<sup>14</sup> School of Physics & Astronomy, Rochester Institute of Technology, 84 Lomb Memorial Drive, Rochester, NY 14623, USA

<sup>15</sup> Instituto de Astrofísica de Andalucía—Consejo Superior de Investigaciones Científicas (CSIC), P.O. Box 3004, E-18008, Granada, Spain

<sup>16</sup> Departamento de Física Teórica, Facultad de Ciencias, Universidad de Zaragoza, E-50019, Zaragoza, Spain

<sup>17</sup> Yale Center for Astronomy and Astrophysics, Yale University, P.O. Box 2018120, New Haven, CT 06520-8120, USA

<sup>18</sup> Gemini Observatory, Northern Operations Center, 670 N. A’ohoku Place, Hilo, HI 96720, USA

<sup>19</sup> Harvard-Smithsonian Center for Astrophysics, 60 Garden Street, Cambridge, MA 02138, USA

Received 2018 August 15; revised 2018 September 13; accepted 2018 September 17; published 2018 October 4

## Abstract

We report spatially resolved [C II]  $\lambda 158 \mu\text{m}$  observations of HE 0433-1028, which is the first detection of a nearby luminous active galactic nucleus (AGN; redshift 0.0355) with the Field-Imaging Far-Infrared Line Spectrometer (FIFI-LS) on board the airborne Stratospheric Observatory For Infrared Astronomy (SOFIA). We compare the spatially resolved star formation tracers [C II], as provided by our SOFIA observations, and  $H\alpha$  from the Multi Unit Spectroscopic Explorer (MUSE) optical integral-field spectroscopy. We find that the [C II] emission is mainly matching the extended star formation as traced by the extinction-corrected  $H\alpha$  line emission but some additional flux is present. While a larger sample is needed to statistically confirm our findings and investigate possible dependencies on AGN luminosity and star formation rate, our study underlines the necessity of collecting a spatially resolved optical–far-infrared data set for nearby AGNs, and shows that it is technically feasible to collect such data sets with FIFI-LS on board SOFIA.

*Key words:* galaxies: active – galaxies: individual (HE 0433-1028) – galaxies: starburst

## 1. Introduction

The [C II] fine-structure line of singly ionized carbon at  $157.74 \mu\text{m}$  is one of the brightest emission lines in the far-infrared and a main cooling line in the interstellar medium and photon-dominated regions (PDR; Hollenbach & Tielens 1999). Many studies show a correlation between the [C II] line and the star formation rate (SFR) in nearby galaxies (e.g., Stacey et al. 1991; Boselli et al. 2002; De Looze et al. 2014; Herrera-Camus et al. 2015). While the optical hydrogen recombination line  $H\alpha$ , another popular star formation rate tracer, is shifted out of the near-infrared at  $z \gtrsim 2$ , the [C II] line shifts to the sub-mm at higher redshift ( $z \gtrsim 4$ , and even  $z \gtrsim 1.5$  in the Atacama Large Millimeter/submillimeter Array (ALMA) band 10) where it can be observed with large interferometers like ALMA or the Northern Extended Millimeter Array (NOEMA) at unprecedented sensitivity and resolution, therefore becoming

a powerful diagnostic for star formation in high-redshift galaxies (e.g., Stacey et al. 2010).

Although the correlation between the [C II] line and the SFR for normal star-forming galaxies is relatively tight, some scatter exists ( $\sim 0.2$  dex, Herrera-Camus et al. 2015) and indicates a mix of different excitation mechanisms in individual galaxies. Of particular interest is which influence the active galactic nucleus (AGN) has on the [C II] luminosity: luminous AGNs have a strong radiation field that is in some cases able to dominate the ionization of the interstellar medium (ISM) even out to kiloparsec scales (e.g., Scharwächter et al. 2011; Husemann et al. 2013) and could therefore contribute to the excitation of  $C^+$  as well. On the other hand, very luminous infrared sources seem to have relatively weaker [C II] luminosities (“C II deficit”). The nature of the main driver of this C II deficit is still an open question (e.g., Smith et al. 2017). Possible explanations for a C II deficit occurring close to the AGN include dust heating by the AGN (e.g., Luhman et al. 2003; Graciá-Carpio et al. 2011) or carbon overionization due to X-rays (e.g., Langer & Pineda 2015; Herrera-Camus et al. 2018). A reliable baseline needs to be established at low

\* Based on observations made with the NASA/DLR Stratospheric Observatory for Infrared Astronomy (SOFIA) and on observations collected at the European Organisation for Astronomical Research in the Southern Hemisphere under ESO programme 094.B-0354(A).

<sup>20</sup> Einstein and Spitzer fellow.

redshift. While some nearby low-luminosity AGN are included in e.g., the KINGFISH survey (Herrera-Camus et al. 2015; Smith et al. 2017), the influence of luminous AGN, as they are ubiquitous at higher redshift, on the calibration of the [C II]-SFR relation needs to be investigated.

Spatially and spectrally resolved analysis is a powerful way to distinguish between extended and central point source emission to estimate the impact of the galactic nucleus. However, this kind of study has not yet been attempted due to the lack of high-spatial and high-spectral resolution observations of reference star formation indicators. The Close AGN Reference Survey (CARS; <http://www.cars-survey.org>, Husemann et al. 2017) comprises a spatially resolved multi-wavelength data set of nearby ( $0.01 < z < 0.06$ ) luminous AGNs that are ideal as a bridge between the well-studied local AGN population and more distant quasi-stellar objects (QSOs; Bertram et al. 2007; Busch et al. 2016). It therefore provides a reference data set for high-redshift galaxies and also offers a range of AGN luminosities ( $L_{\text{bol}} \sim 10^{43}\text{--}10^{45.5} \text{ erg s}^{-1}$ ) that allows for a statistical analysis of possible deviations from the [C II]-SFR relation as a function of the AGN luminosity.

In this Letter we report the first spatially resolved detection of [C II] line emission in a nearby luminous AGN with the airborne Stratospheric Observatory For Infrared Astronomy (SOFIA; Young et al. 2012). We test the [C II]-SFR relation in the presence of a bright AGN by comparing spatially resolved [C II] emission with respect to  $\text{H}\alpha$  as a reference SFR indicator. HE 0433-1028 is a strongly barred spiral galaxy at a redshift of  $z = 0.0355$  and an AGN luminosity of  $4 \times 10^{44} \text{ erg s}^{-1}$ . Adopting a cosmology with  $H_0 = 70 \text{ km s}^{-1} \text{ Mpc}^{-1}$ ,  $\Omega_{\text{M}} = 0.3$  and  $\Omega_{\Lambda} = 0.7$ , the redshift corresponds to a luminosity distance of  $D_L = 157.4 \text{ Mpc}$  and a scale of  $0.707 \text{ kpc}''$ .

## 2. Observations

### 2.1. FIFI-LS Far-infrared 3D Spectroscopy

The Field-Imaging Far-Infrared Line Spectrometer (FIFI-LS; Klein et al. 2010; Fischer et al. 2018) on board the flying telescope SOFIA is an integral-field spectrograph working at far-infrared wavelengths. The AGN HE 0433-1028 was observed on 2016 March 1 at a pressure altitude of 39,000 feet, with an on-source total exposure time of 25.6 minutes. We used the red channel centered on the [C II]  $\lambda 157.7 \mu\text{m}$  line (redshifted with  $z = 0.0355$ ), providing a spectral coverage from  $162.8 \mu\text{m}$  to  $163.9 \mu\text{m}$ . In this mode, the array consists of  $5 \times 5$  pixels with a pixel size of  $12'' \times 12''$  each. The spectral resolution is  $R \approx 1200$  or  $250 \text{ km s}^{-1}$  at this wavelength.

Chop-subtraction, flat correction, telluric correction, flux calibration, and spectral rebinning is performed by the instrument pipeline. Before spatial rebinning, we calculate and subtract the remaining background in each exposure and spatial position by calculating a weighted average of the spectral region around the expected emission line. In this process we also calculate the standard deviation. In the next step, we replace NaN-values in the spectrum with white noise with the previously calculated standard deviation. This ensures a constant noise over the whole spectral range. The spatial alignment and rebinning to a pixel size of  $12'' \times 12''$  is done with a Drizzle algorithm (Fruchter & Hook 2002).

While coadding the drizzled cubes, we realized that not all cubes have the same quality. We therefore decided to observe how the signal-to-noise ratio (S/N) of the line detection

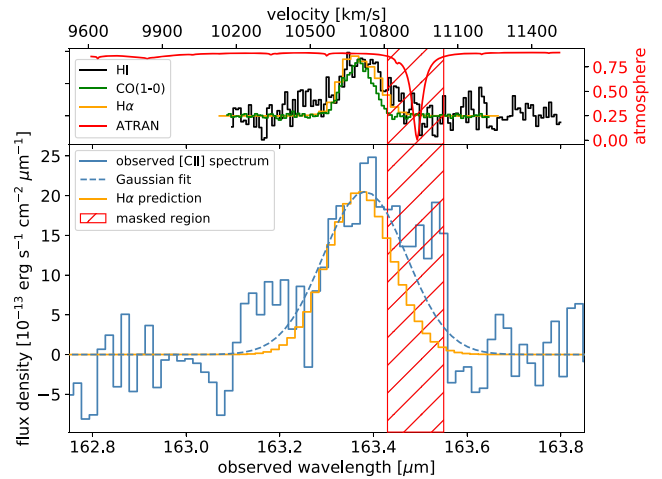


**Figure 1.** Bottom panel: FIFI-LS spectrum integrated in an aperture with radius  $18''$  (blue line), approximately corresponding to the FWHM of the PSF. A region masked in the fit because of low atmospheric transmission is marked with red stripes. A Gaussian fit of the [C II] line, which has an S/N of  $\sim 18$ , is shown in dashed lines. The orange spectrum shows the expected line profile, based on  $\text{H}\alpha$  observations. Top panel: integrated H I, CO(1-0) and  $\text{H}\alpha$  line profile. A synthetic spectrum of the atmospheric transmission from ATRAN is overlaid in red. It is apparent that no emission is expected in the spectral region with low atmospheric transmission.

behaves while adding more cubes. It became apparent that only during the second half of the observation, the increase of S/N with cumulative exposure time  $t_{\text{exp}}$  followed the expected relation  $\text{S/N} \propto \sqrt{t_{\text{exp}}}$ . During the first half of the observations, the S/N stayed constant over time on a low level. We therefore concluded that the cubes observed during the first half were not useful due to technical or weather influence (higher line-of-sight water vapor forecasted at the beginning of flight leg) and only coadded the second half. This left us with 25 accepted and 25 rejected frames, resulting in an effective exposure time of about 13 minutes.

Figure 1 (bottom panel, blue line) shows the resulting FIFI-LS spectrum integrated in the central aperture with radius  $18''$ , which roughly corresponds to the FWHM of the point-spread function (PSF) of the SOFIA telescope. In orange, we show the scaled  $\text{H}\alpha$  line (see below), integrated over the same aperture. Beforehand, the Multi Unit Spectroscopic Explorer (MUSE)  $\text{H}\alpha$  datacube was smoothed and regridded to match the spatial resolution of SOFIA and spectral resolution of FIFI-LS (see also Section 3). In the top panel, we show the line profiles of H I (Nançay radio telescope; Davoust & Contini 2004), CO(1-0) (ALMA; T. Davis 2018, private communication), and  $\text{H}\alpha$ , and overlay in red a synthetic spectrum of the atmospheric transmission created with ATRAN<sup>21</sup> (Lord 1992). The CO and  $\text{H}\alpha$  spectra were extracted over the same area as the [C II] observation, while the H I observation had a much larger beam of several arcmin. We see that there is a strong absorption feature at  $163.5 \mu\text{m}$ , but we do not expect any emission in neutral and ionized gas at the velocity of this feature. However, this feature might cause strong residuals in the [C II] emission. We therefore decide to mask this spectral region (red stripes in Figure 1) before fitting a Gaussian function that we show as a dashed line in the bottom panel of Figure 1. The fitted [C II] line has an S/N of  $\sim 18$ . The line width is  $\text{FWHM} \approx 380 \text{ km s}^{-1}$  ( $290 \text{ km s}^{-1}$

<sup>21</sup> <https://atran.sofia.usra.edu/>

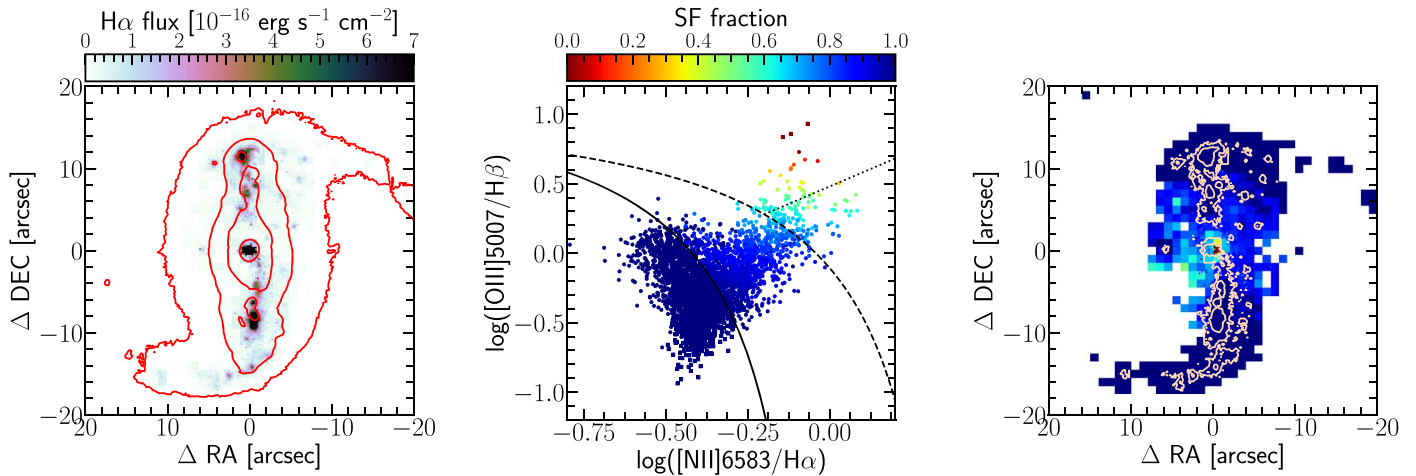


**Figure 2.** Left panel: AGN-subtracted and extinction-corrected H $\alpha$  flux map that traces the star formation in the galaxy with high resolution.  $i$ -band continuum emission is overlaid in red contours. The H $\alpha$  emission shows an elongated distribution as the star formation regions are mostly situated within the stellar bar. Middle panel: optical Baldwin, Phillips & Terlevich (BPT) diagram (with division lines from Kewley et al. 2001; Kauffmann et al. 2003; Cid Fernandes et al. 2010) showing the ionization mechanisms of the nebular gas on a spaxel-to-spaxel basis. The AGN fraction is color coded with red being purely excited by AGN and blue purely by star formation. Right panel: map of the AGN fraction, with H $\alpha$  contours overlaid. The flux in each pixel of HaMap is lowered by the respective AGN fraction to resemble the extended emission based on star formation.

after correcting for instrumental resolution) and the peak velocity of the [C II] emission coincides with that of the H $\alpha$  line within  $\lesssim 30 \text{ km s}^{-1}$ . This demonstrates FIFI-LS ability to detect extragalactic sources, and extends SOFIA’s scope from sources in the immediate Galactic neighborhood to nearby galaxies and AGNs.

## 2.2. MUSE Optical 3D Spectroscopy

Optical integral-field spectroscopy with MUSE (Bacon et al. 2010) is available from CARS. HE 0433-1028 was observed in 2014 December with a total on-source integration time of 600 s. The reduction with the standard ESO pipeline Weilbacher et al. (2012) results in a datacube with a large field-of-view (FOV) of  $1' \times 1'$  which matches the FIFI-LS FOV. The spatial scaling is  $0''.2$  per spaxel (spatial pixel) and the wavelength coverage is 4750–9300 Å with a spectral resolution of  $R = 2500$  ( $\sim 110 \text{ km s}^{-1}$ ) at the wavelength of the H $\alpha$  line.

The tool QDeblend<sup>3D</sup> makes use of the fact that HE 0433-1028 is an unobscured AGN and the broad-line region appears point-like. By combining spatial and spectral information, it is possible to deblend central point-like and extended emission in an iterative process (Husemann et al. 2014). In a next step, the stellar continuum was subtracted and optical emission lines were fitted with Gaussian functions across the cube. Using the Balmer decrement  $\text{H}\alpha/\text{H}\beta$ , extinction correction was then performed following the extinction law of Cardelli et al. (1989). Figure 2 (left panel) shows a map of the extinction-corrected H $\alpha$  extended emission with the  $i$ -band continuum emission overlaid as contours.

We then analyze the excitation mechanisms of the ionized gas across the galaxy. We show the Baldwin, Phillips & Terlevich (BPT) diagram (Baldwin et al. 1981), which uses the ratios of nearby optical emission lines to distinguish the ionization mechanism of nebular gas (Figure 2, middle panel). In the diagram, we fit a straight mixing line in linear-linear space. The H II and narrow-line region AGN basis spectra are the ones with line ratios closest to the minimal and maximal points of this line. Assuming that all of the spectra are a linear

combination of the H II and AGN basis spectra, we can now derive the AGN and star-forming fraction (Davies et al. 2016). The color coding shows the AGN fraction for each pixel. The right panel shows the AGN fractions in the map. The H $\alpha$  flux in each pixel is then lowered by the respective AGN fraction. This leaves us with an AGN-subtracted H $\alpha$  map which is representative of the extended star formation.

## 3. Modeling the [C II] Emission

With the available FIFI-LS data we can spatially distinguish between the central region that might be influenced by the AGN and the star formation along the bar. In Figure 3, fourth panel, we show the flux distribution of the [C II] line, which we derive by summing up the spectra on a spaxel-by-spaxel basis between  $163.2 \mu\text{m}$  and  $163.43 \mu\text{m}$ . The first value was chosen based on the H $\alpha$  spectrum and the fit described in Section 2.1,<sup>22</sup> the latter value was chosen to avoid the atmospheric absorption feature (see Figure 1). We correct for missing flux in this wing by applying a correction factor of 1.5, which was derived from the integrated spectrum by comparing the total flux in the Gaussian with the flux derived when summing only in the mentioned interval. The resulting map resembles the elongated structure of the star-forming regions in the bar, as visible in the H $\alpha$  map in Figure 2 (left panel), which has a length of about  $30''$  ( $\sim 20 \text{ kpc}$ ). When considering only pixels with  $\text{S/N} > 3$ , we find an extent of almost  $1'$ . However, the length is affected by beam smearing. To further quantify this finding, we aim at distinguishing between extended emission and unresolved point source contribution. However, given the small extent of the galaxy ( $\sim 30''$ ) compared to the spatial resolution of SOFIA ( $\sim 13''$ ), a direct decomposition seems inadvisable. Instead, we use a forward modeling approach with the MUSE H $\alpha$  map as a high spatial-resolution prior, which is also not affected by beam-smearing. Our model consists of two components: extended emission and an unresolved point source.

<sup>22</sup> We confirmed that changing the starting value to e.g.,  $163.1 \mu\text{m}$  leads to the same results within the uncertainties.

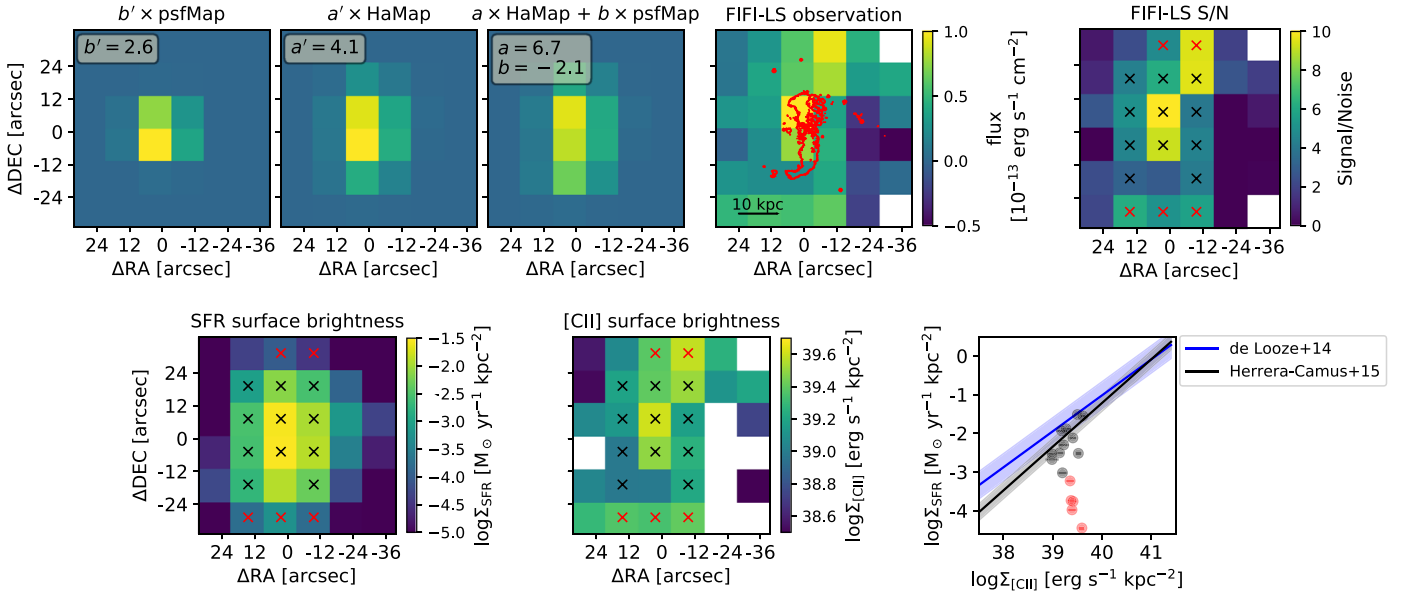


**Figure 3.** From left to right, top row: we compare three different models, only point source, only extended emission and a combined model, each fitted to the observed [C II] line map from FIFI-LS obtained by integrating over the wavelength interval from  $163.2 \mu\text{m}$  to  $163.43 \mu\text{m}$ . It becomes apparent that the line distribution is extended. In the fourth panel we show the observed [C II] emission line map with contours of  $\text{H}\alpha$  from the MUSE cube overlaid in red. In the last panel we show the S/N map of our observations. Pixels with  $\text{S/N} > 3$  are marked with crosses. Bottom row: surface brightnesses of star formation rate and [C II] emission. Spatially resolved [C II]-SFR relation, with relations from the literature indicated.

For the extended emission, HaMap, we use the extinction-corrected  $\text{H}\alpha$  flux map (see Figure 2) as a prior for the expected [C II], assuming that both trace the gas excitation from star formation. We convolve the  $\text{H}\alpha$  map with the spatial resolution of SOFIA’s 2.7m-telescope (PSF approximated with a Gaussian with  $\text{FWHM} \approx 12''$  at  $163.4 \mu\text{m}$ ) and apply a spatial rebinning to a  $12''$  pixel grid as implied by the SOFIA data with respect to the target coordinates. We stress that the AGN-host galaxy deblending step as described in Section 2.2 is essential for using the  $\text{H}\alpha$  maps as a robust star formation tracer.

The spatially unresolved component, psfMap, aims to account for a possible point source contribution to the [C II] flux. Here we assume a simple 2D Gaussian model for the PSF of the SOFIA telescope with  $\text{FWHM} \approx 12''$  at the observed [C II] wavelength. In Figure 3, first and second panel, we show maps of the two components, both scaled to the observed map (fourth panel) by minimizing the least-square error between observation and model. It becomes apparent that the emission is extended and a point source is not a good representation. The scaling factors, when using only single components, are  $a' = 4.1$  for the extended emission and  $b' = 2.6$  for the point source model.

The full model is given by a linear combination  $a \times \text{HaMap} + b \times \text{psfMap}$ . Because we normalize both reference maps to a total flux of 1, the scaling factors  $a$  and  $b$  denote the flux of the extended [C II] emission and the point source emission, respectively, in units of  $10^{-13} \text{ erg s}^{-1} \text{ cm}^{-2}$ . To find the best-fit parameters of this model, including their  $1\sigma$  uncertainties, we use the Markov-Chain Monte-Carlo code EMCEE (Foreman-Mackey et al. 2013). Figure 4 is a visualization of the explored parameter space, the resulting map is shown in Figure 3, third panel. The best fit parameters are  $a = 6.7 \pm 0.7$  and  $b = -2.1 \pm 0.5$ ; this indicates that the extended emission is the dominating component and an

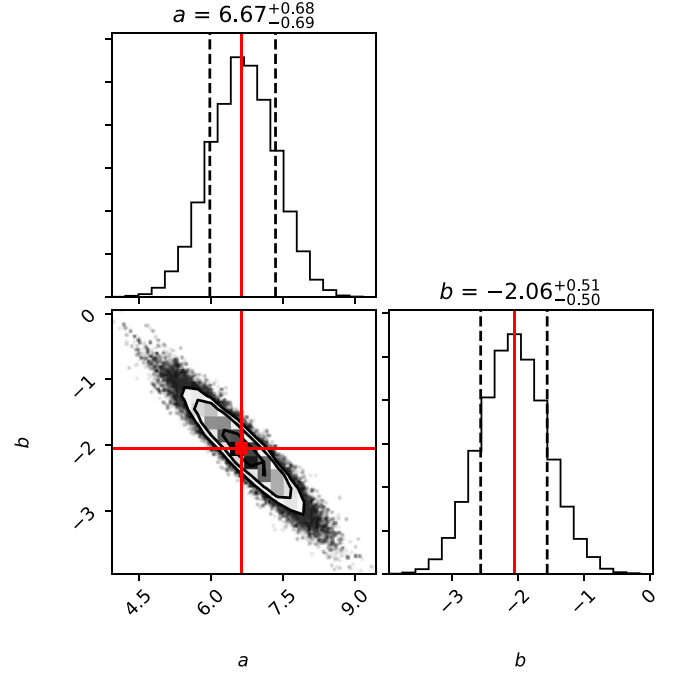


**Figure 4.** Corner-plot visualization (Foreman-Mackey 2016) of the parameter space explored by our model-fitting procedure.  $a$  and  $b$  denote the fitted flux of the extended emission and the point source emission, respectively. The histograms show the marginalized posterior distribution of the parameters, and the dashed vertical lines indicate the  $1\sigma$  confidence intervals. Red lines show the maximum likelihood parameters.

additional small negative point source contribution is favored by the model.

The total [C II] flux indicated by the model is  $4.6 \times 10^{-13} \text{ erg s}^{-1} \text{ cm}^{-2}$ , the same as the flux derived from the Gaussian fit of the integrated spectrum. Comparing with the total extinction-corrected  $\text{H}\alpha$  flux of  $5.6 \times 10^{-13} \text{ erg s}^{-1} \text{ cm}^{-2}$ , we derive a flux ratio of  $f_{\text{[C II]}}/f_{\text{H}\alpha} \sim 0.8$ . Assuming a linear

$L_{[\text{C II}]}-L_{\text{H}\alpha}$  relation, we connect the linear  $L_{[\text{C II}]}-L_{\text{SFR}}$  relation from Herrera-Camus et al. (2015) with the linear  $L_{\text{H}\alpha} - \text{SFR}$  relation (Kennicutt & Evans 2012); this leads to a predicted relation of  $L_{[\text{C II}]} = 1.1 \times L_{\text{H}\alpha}$ , which is consistent with our result.

The modeled total [C II] flux corresponds to a [C II] luminosity of  $L_{[\text{C II}]} = 3.5 \times 10^8 L_{\odot}$ . Using the calibration of Herrera-Camus et al. (2015), who report a scatter of  $\sim 0.2$  dex, we obtain a star formation rate of  $\sim 8.4 M_{\odot} \text{ yr}^{-1}$ , which agrees very well with the star formation estimate from the AGN-subtracted and dust-corrected  $\text{H}\alpha$  luminosity of  $\sim 8.9 M_{\odot} \text{ yr}^{-1}$  (Kennicutt & Evans 2012).

As the magnitude  $a = 6.7 \pm 0.7$  of the extended emission is significantly higher than the magnitude of the point source contribution  $b = -2.1 \pm 0.5$ , we conclude that the extended emission is the dominating contribution to the [C II] flux. However, as also visible in the maps in Figure 3, a point-like contribution is required. A negative point source contribution could indicate that the central [C II] emission is reduced in the presence of an AGN, for example due to overionization of the emitting gas (e.g., Langer & Pineda 2015). This could also hint at different star formation rates in bar and bulge, of which the latter cannot be spatially separated from an AGN component at the resolution of SOFIA.

In the top row of Figure 3 we show a map of the model together with maps of the two components separately. These maps are directly compared to the aforementioned map of the observed emission. In the bottom row of Figure 3 we show surface brightnesses of star formation and [C II] emission. At  $\text{S/N} > 3$  (indicated with crosses in the maps), we detect an elongated bar-like structure with an extend of almost one arcminute. We place the pixels with  $\text{S/N} > 3$  in the  $\Sigma_{[\text{C II}]}-\Sigma_{\text{SFR}}$  relation next to the maps. It becomes apparent that in the central pixels the [C II] emission follows the  $\text{H}\alpha$  emission and lies on published  $\Sigma_{[\text{C II}]}-\Sigma_{\text{SFR}}$  relations (De Looze et al. 2014; Herrera-Camus et al. 2015). Therefore, we can conclude that, within the galaxy, [C II] predominantly traces star formation excited PDRs. In the North and South of the galaxy, however, we observe additional [C II] emission that is not following the  $\text{H}\alpha$  and CO emission. We suspect that the [C II] emission there is a trace of the cold neutral medium (CNM), of which [C II] is the dominant cooling process and which can be excited by many processes including the ultraviolet (UV) background and cosmic rays (e.g., Wolfire et al. 2003). While in the centers of galaxies PDRs are the main contributor to [C II], in the outskirts of galaxies the CNM can contribute significantly to the [C II] emission (see e.g., in M33; Kramer et al. 2013). Consistent with this, the velocities of the emission in these regions are contained in the spectrum of H I, which is the main tracer of the CNM.

In Figure 5, we show the position of HE 0433-1028 in the  $L_{[\text{C II}]} / L_{\text{FIR}} - L_{\text{CO}(1-0)} / L_{\text{FIR}}$  diagram (Stacey et al. 2010, and references therein). The far-infrared luminosity is  $L_{\text{FIR}} = 1.1 \times 10^{11} L_{\odot}$  (derived in Moser et al. 2016), which indicates that the [C II] contributes around 0.5% to the far-infrared luminosity. The integrated emission of the  $^{12}\text{CO}(1-0)$  transition, mapped with ALMA (T. Davis 2018, private communication), has a flux of  $(58.05 \pm 1.08) \text{ Jy km s}^{-1}$  that corresponds to a luminosity of  $L_{\text{CO}} = 1.74 \times 10^5 L_{\odot}$ . This is consistent with previous single-dish CO-observations with the IRAM-30 m telescope (Bertram et al. 2007), yielding a luminosity of the  $^{12}\text{CO}(1-0)$  line of  $L_{\text{CO}} = 1.1 \times 10^5 L_{\odot}$ , which is  $\sim 30\%$  lower

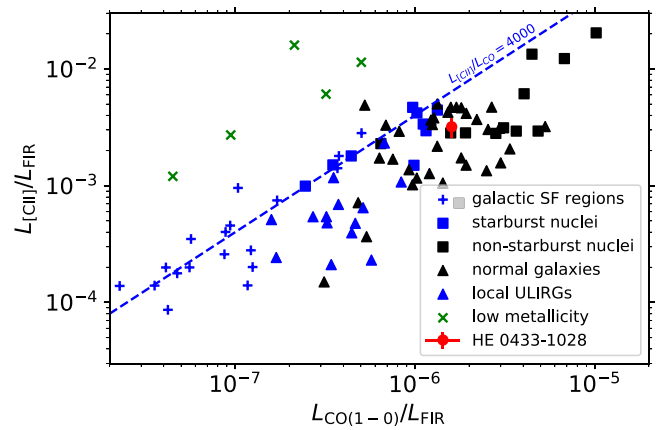


**Figure 5.** Position of HE 0433-1028 in the  $L_{\text{CO}(1-0)}/\text{FIR} - L_{[\text{C II}]} / L_{\text{FIR}}$  plane compared to data points for normal galaxies, ultraluminous infrared galaxies, galactic star formation regions, galactic nuclei, and low-metallicity galaxies from Stacey et al. (2010) and De Breuck et al. (2011, and references therein). A typical starburst [C II]/CO line ratio of  $\sim 4000$  is indicated.

because the galaxy is more extended than the IRAM-30 m beam.

The line ratio between the [C II] and the  $^{12}\text{CO}(1-0)$  line is often used as a diagnostic of the star formation activity in galaxies. While the [C II] line scales strongly with the far-UV radiation emitted by young OB stars, the  $\text{CO}(1-0)$  stems from better shielded regions. Therefore, starburst-dominated regions show higher [C II]/CO ratios. Typical ratios of starburst galaxies are of the order of  $\sim 4000$  and can reach up to a few  $10^4$  in extreme cases, but are by a factor of 3 smaller in non-starburst nuclei (Stacey et al. 1991). Also, in low-metallicity galaxies, higher  $L_{[\text{C II}]} / L_{\text{FIR}}$  and  $L_{[\text{C II}]} / L_{\text{CO}}$  ratios than in normal galaxies are observed (e.g., Madden 2000; Röllig et al. 2006; Cormier et al. 2015), which are explained by larger  $\text{C}^+$ -emitting regions. For HE 0433-1028, we measure a line ratio of  $L_{[\text{C II}]} / L_{\text{CO}} \sim 2030$ , which is a typical value. A more detailed analysis of possible metallicity gradients will be pursued with spatially resolved CO data. This underlines the necessity for multi-wavelength observations with high spatial resolution.

#### 4. Summary and Conclusions

In this Letter, we presented integral-field spectroscopy observations of the [C II]  $\lambda 158 \mu\text{m}$  emission line of the nearby luminous AGN HE 0433-1028 at a redshift of 0.0355. This is the first spatially resolved far-infrared observation of a nearby luminous AGN and the object with the highest redshift that has been studied with the airborne observatory SOFIA so far.

Compared to high- $z$  QSOs, HE 0433-1028 is still close enough to resolve separate star formation regions (Busch et al. 2015). This makes sources like HE 0433-1028 ideal targets to analyze a star-forming galaxy in the presence of a strong AGN and study the counterplay of star formation and AGN activity.

We can clearly resolve the elongated structure of the star-forming regions along the large-scale bar. We compare the data to a model that consists of an extended emission and point source component, both based on a high-resolution AGN-subtracted  $\text{H}\alpha$ -map. The model fit suggests that the [C II] follows the extended ( $30'' \approx 20 \text{ kpc}$ )  $\text{H}\alpha$  emission, which is excited by star formation. An additional small negative point source component is suggested by the model. However, a dependency of the point source contribution on the AGN

luminosity or other parameters has to be verified with a larger sample.

Previous studies (e.g., Sargsyan et al. 2014) have already suggested that [C II] can serve as a star formation estimator also in AGNs, but only with a precision of  $\sim 50\%$ . However, because they were comparing integrated measurements, it was not clear whether or not increased scatter comes from an additional component associated with the AGN, or globally different scaling factors between [C II] and SFR. With our spatially resolved [C II] observations and  $H\alpha$  comparison data, we see that in HE 0433-1028 the extended emission of [C II] and  $H\alpha$  are statistically matching and yield scaling factors consistent with inactive galaxies, with an additional flux excess North and South of the bar. While integrated [C II]/CO line ratios indicate a metallicity typical for normal galaxies, possible metallicity variations will be analyzed in more detail with upcoming spatially resolved optical and CO measurements.

While the sole purpose of this Letter is to demonstrate the feasibility of spatially resolved analysis of [C II] emission in nearby luminous AGNs, with reasonable observing time effort, the upcoming observations of a larger set of in total five quasi-stellar objects with different AGN luminosities from the CARS survey will allow us to probe the [C II]-SFR connection as a function of AGN luminosity and SFR.

Based in part on observations made with the NASA/DLR Stratospheric Observatory for Infrared Astronomy (SOFIA). SOFIA is jointly operated by the Universities Space Research Association, Inc. (USRA), under NASA contract NAS2-97001, and the Deutsches SOFIA Institut (DSI) under DLR contract 50 OK 0901 to the University of Stuttgart. We thank the anonymous referee for a constructive report that helped to clarify the manuscript. This work was supported by the Deutsche Forschungsgemeinschaft (DFG) via SFB 956, subprojects A2, and A6. The work of S.B. and C.O. was supported by NSERC (Natural Sciences and Engineering Research Council of Canada). M.G. is supported by NASA through Einstein Postdoctoral Fellowship Award No. PF5-160137 issued by the *Chandra* X-ray Observatory Center, which is operated by the SAO for and on behalf of NASA under contract NAS8-03060. Support for this work was also provided by *Chandra* grant GO7-18121X. M.K. acknowledges support by DLR 50OR1802. M.P.T. acknowledges support from the Spanish MINECO through grants AYA2012-38491-C02-02 and AYA2015-63939-C2-1-P.

#### ORCID iDs

G. Busch  <https://orcid.org/0000-0001-6679-5481>  
 B. Husemann  <https://orcid.org/0000-0003-2901-6842>  
 I. Smirnova-Pinchukova  <https://orcid.org/0000-0002-2260-3043>  
 A. Eckart  <https://orcid.org/0000-0001-6049-3132>  
 S. A. Baum  <https://orcid.org/0000-0002-4735-8224>  
 F. Combes  <https://orcid.org/0000-0003-2658-7893>  
 S. M. Croom  <https://orcid.org/0000-0003-2880-9197>  
 T. A. Davis  <https://orcid.org/0000-0003-4932-9379>  
 N. Fazeli  <https://orcid.org/0000-0001-7163-536X>

C. Fischer  <https://orcid.org/0000-0003-2649-3707>  
 M. Gaspari  <https://orcid.org/0000-0003-2754-9258>  
 R. Klein  <https://orcid.org/0000-0002-7187-9126>  
 R. McElroy  <https://orcid.org/0000-0003-2290-7060>  
 C. P. O’Dea  <https://orcid.org/0000-0001-6421-054X>  
 M. A. Perez-Torres  <https://orcid.org/0000-0001-5654-0266>  
 Á. Sánchez-Monge  <https://orcid.org/0000-0002-3078-9482>  
 J. Scharwächter  <https://orcid.org/0000-0003-1585-9486>  
 G. R. Tremblay  <https://orcid.org/0000-0002-5445-5401>  
 T. Urrutia  <https://orcid.org/0000-0001-6746-9936>

#### References

- Bacon, R., Accardo, M., Adjali, L., et al. 2010, *Proc. SPIE*, 7735, 773508  
 Baldwin, J. A., Phillips, M. M., & Terlevich, R. 1981, *PASP*, 93, 5  
 Bertram, T., Eckart, A., Fischer, S., et al. 2007, *A&A*, 470, 571  
 Boselli, A., Gavazzi, G., Lequeux, J., & Pierini, D. 2002, *A&A*, 385, 454  
 Busch, G., Fazeli, N., Eckart, A., et al. 2016, *A&A*, 587, A138  
 Busch, G., Smajić, S., Scharwächter, J., et al. 2015, *A&A*, 575, A128  
 Cardelli, J. A., Clayton, G. C., & Mathis, J. S. 1989, *ApJ*, 345, 245  
 Cid Fernandes, R., Stasińska, G., Schlickmann, M. S., et al. 2010, *MNRAS*, 403, 1036  
 Cormier, D., Madden, S. C., Lebouteiller, V., et al. 2015, *A&A*, 578, A53  
 Davies, R. L., Groves, B., Kewley, L. J., et al. 2016, *MNRAS*, 462, 1616  
 Davoust, E., & Contini, T. 2004, *A&A*, 416, 515  
 De Breuck, C., Maiolino, R., Caselli, P., et al. 2011, *A&A*, 530, L8  
 De Looze, I., Cormier, D., Lebouteiller, V., et al. 2014, *A&A*, 568, A62  
 Fischer, C., Beckmann, S., Bryant, A., et al. 2018, *JAI*, 7, 1840003  
 Foreman-Mackey, D. 2016, corner.py: Scatterplot matrices in Python, Journal of Open Source Software, 1, 24, doi:10.21105/joss.00024  
 Foreman-Mackey, D., Hogg, D. W., Lang, D., & Goodman, J. 2013, *PASP*, 125, 306  
 Fruchter, A. S., & Hook, R. N. 2002, *PASP*, 114, 144  
 Graciá-Carpio, J., Sturm, E., Hailey-Dunsheath, S., et al. 2011, *ApJL*, 728, L7  
 Herrera-Camus, R., Bolatto, A. D., Wolfire, M. G., et al. 2015, *ApJ*, 800, 1  
 Herrera-Camus, R., Sturm, E., Graciá-Carpio, J., et al. 2018, *ApJ*, 861, 95  
 Hollenbach, D. J., & Tielens, A. G. G. M. 1999, *RvMP*, 71, 173  
 Husemann, B., Jahnke, K., Sánchez, S. F., et al. 2014, *MNRAS*, 443, 755  
 Husemann, B., Tremblay, G., Davis, T., et al. 2017, *Msngr*, 169, 42  
 Husemann, B., Wisotzki, L., Sánchez, S. F., & Jahnke, K. 2013, *A&A*, 549, A43  
 Kauffmann, G., Heckman, T. M., Tremonti, C., et al. 2003, *MNRAS*, 346, 1055  
 Kennicutt, R. C., & Evans, N. J. 2012, *ARA&A*, 50, 531  
 Kewley, L. J., Dopita, M. A., Sutherland, R. S., Heisler, C. A., & Trevena, J. 2001, *ApJ*, 556, 121  
 Klein, R., Poglitsch, A., Raab, W., et al. 2010, *Proc. SPIE*, 7735, 77351T  
 Kramer, C., Abreu-Vicente, J., García-Burillo, S., et al. 2013, *A&A*, 553, A114  
 Langer, W. D., & Pineda, J. L. 2015, *A&A*, 580, A5  
 Lord, S. D. 1992, A New Software Tool for Computing Earth’s Atmospheric Transmission of Near- and Far-infrared Radiation, NASA Technical Memorandum 103957  
 Luhman, M. L., Satyapal, S., Fischer, J., et al. 2003, *ApJ*, 594, 758  
 Madden, S. C. 2000, *NewAR*, 44, 249  
 Moser, L., Krips, M., Busch, G., et al. 2016, *A&A*, 587, A137  
 Röllig, M., Ossenkopf, V., Jeyakumar, S., Stutzki, J., & Sternberg, A. 2006, *A&A*, 451, 917  
 Sargsyan, L., Samsonyan, A., Lebouteiller, V., et al. 2014, *ApJ*, 790, 15  
 Scharwächter, J., Dopita, M. A., Zuther, J., et al. 2011, *AJ*, 142, 43  
 Smith, J. D. T., Croxall, K., Draine, B., et al. 2017, *ApJ*, 834, 5  
 Stacey, G. J., Geis, N., Genzel, R., et al. 2019, *ApJ*, 373, 423  
 Stacey, G. J., Hailey-Dunsheath, S., Ferkinhoff, C., et al. 2010, *ApJ*, 724, 957  
 Weilbacher, P. M., Streicher, O., Urrutia, T., et al. 2012, *Proc. SPIE*, 8451, 84510B  
 Wolfire, M. G., McKee, C. F., Hollenbach, D., & Tielens, A. G. G. M. 2003, *ApJ*, 587, 278  
 Young, E. T., Becklin, E. E., Marcum, P. M., et al. 2012, *ApJL*, 749, L17